

Scattering makes a difference in circular dichroic angle-resolved photoemission

Honey Boban ^{1,2}, Mohammed Qahosh ¹, Xiao Hou ^{1,2}, Tomasz Sobol ³, Edyta Beyer ³, Magdalena Szczepanik ³, Daniel Baranowski ¹, Simone Mearini ¹, Vitaliy Feyer ¹, Yuriy Mokrousov ^{4,5}, Yishui Zhou ⁶, Yixi Su ⁶, Keda Jin ^{7,2,8}, Tobias Wichmann ^{7,2,9}, Jose Martinez-Castro ^{7,2}, Markus Ternes ^{7,8,2}, F. Stefan Tautz ^{7,9}, Felix Lüpke ⁷, Claus M. Schneider ^{1,10,11}, Jürgen Henk ¹² and Lukasz Plucinski ^{1,8,*}

¹Peter Grünberg Institut (PGI-6), Forschungszentrum Jülich GmbH, 52428 Jülich, Germany

²JARA-FIT (Fundamentals of Future Information Technology), Jülich-Aachen Research Alliance, Forschungszentrum Jülich and RWTH Aachen University, 52425 Jülich, Germany

³National Synchrotron Radiation Centre SOLARIS, Jagiellonian University, 30-392 Kraków, Poland

⁴Peter Grünberg Institut (PGI-1), Forschungszentrum Jülich GmbH, 52428 Jülich, Germany

⁵Institute of Physics, Johannes Gutenberg University Mainz, 55099 Mainz, Germany

⁶Jülich Centre for Neutron Science (JCNS) at Heinz Maier-Leibnitz Zentrum (MLZ), Forschungszentrum Jülich, Lichtenbergstrasse 1, D-85747 Garching, Germany

⁷Peter Grünberg Institut (PGI-3), Forschungszentrum Jülich GmbH, 52428 Jülich, Germany

⁸Institute for Experimental Physics II B, RWTH Aachen University, 52074 Aachen, Germany

⁹Institute for Experimental Physics IV A, RWTH Aachen University, 52074 Aachen, Germany

¹⁰Fakultät für Physik, Universität Duisburg-Essen, 47048 Duisburg, Germany

¹¹Physics Department, University of California, Davis, California 95616, USA

¹²Institut für Physik, Martin-Luther-Universität Halle-Wittenberg, 06099 Halle (Saale), Germany



(Received 16 November 2024; revised 6 February 2025; accepted 10 February 2025; published 11 March 2025)

Recent years have witnessed a steady progress towards blending two-dimensional quantum materials into technology, with future applications often rooted in the electronic structure. Since crossings and inversions of electronic bands with different orbital characters determine intrinsic quantum transport properties, knowledge of the orbital character is essential. Here, we benchmark angle-resolved photoelectron emission spectroscopy (ARPES) as a tool to experimentally derive orbital characters. For this purpose we study the valence electronic structure of two technologically relevant quantum materials, graphene and WSe_2 , and focus on circular dichroism that is believed to provide sensitivity to the orbital angular momentum. We analyze the contributions related to angular atomic photoionization profiles, interatomic interference, and multiple scattering. Regimes in which initial-state properties could be disentangled from the ARPES maps are critically discussed and the potential of using circular dichroic ARPES as a tool to investigate the spin polarization of initial bands is explored. For the purpose of generalization, results from two additional materials, GdMn_6Sn_6 and PtTe_2 , are presented in addition. This research demonstrates rich complexity of the underlying physics of circular dichroic ARPES, providing insights that will shape the interpretation of both past and future circular-dichroic ARPES studies.

DOI: [10.1103/PhysRevB.111.115127](https://doi.org/10.1103/PhysRevB.111.115127)

I. INTRODUCTION AND MOTIVATION

Detailed understanding of quantum materials is a foundation upon which future information technologies will be based. Some of the key phenomena along this path are related to an intimate relation between the electronic band structure and transport properties where orbital and spin character band inversions play a key role. In particular, regions of avoided band crossings with mixed orbital angular momenta (OAM)

and mixed spin characters contribute to a nonvanishing Berry curvature, an integral of which throughout the Brillouin zone (BZ) determines the conductivity within the Kubo linear response formalism. Recently, a new field, known as orbitronics and dealing with detection, manipulation, and dynamics of OAM of electrons in solids, has emerged and is rapidly advancing [1]. Since light does not directly couple to electron spin, the spin sensitivity of experimental techniques such as magneto-optical Kerr rotation and x-ray magnetic circular dichroism is a consequence of light coupling with the OAM via spin-orbit coupling (SOC). The influence of OAM-related processes goes as far as an alternative explanation [2] of the celebrated spin-Hall experiment [3].

Circular dichroic angle-resolved photoemission (CD-ARPES) has been broadly used to reveal OAM-related effects in dispersive valence bands. An incomplete list includes studying the orbital Rashba effect [4], chiral orbital angular

*Contact author: l.plucinski@fz-juelich.de

momenta in topological surface states [5], spin textures of topological surface states [6], OAM textures in the surface states of WTe₂ [7], Berry curvatures of spin-momentum-locked bands [8–10], OAM textures in topological Kondo insulators [11], signatures of a spin-orbital chiral metal [12], time-reversal symmetry breaking in an altermagnet [13], and an OAM texture of indenene [14]. For orbitronics, proper identification of OAM of electronic states from CD-ARPES is of utmost importance, as it governs fundamental nonequilibrium effects such as orbital currents [1] and orbital pumping [15], the orbital Hall effect [16], orbital relaxation [17], laser-induced orbital magnetization [18], and even the phenomenon of ultrafast magnetization dynamics [19–21].

While well understood for atoms [22], where it has been termed *circular dichroism in angular distribution* (CDAD), CD-ARPES, as a fundamental probe of electronic structures with its relation to the OAM and spin characters of the electronic states, remains to be thoroughly understood in solids. CD-ARPES is influenced by several key contributions, including the initial-state orbital angular momentum (OAM), multiple scattering effects such as the Daimon effect, and spin-orbit scattering (for states that are spin polarized). To date, no dedicated studies have been conducted to disentangle these contributions or establish their relative magnitudes in the CD-ARPES signal.

Numerous fundamental properties of solids can be derived from the quantum geometric tensor (QGT) [23], making experimental access to it a pressing challenge in condensed matter physics [24,25]. In photoemission studies, the initial-state wave functions are often expressed within the tight-binding approximation as

$$\psi_i(\mathbf{k}) = \sum_j C_j(\mathbf{k}) \cdot \phi_j, \quad (1)$$

where $j \in \{\mathbf{r}_j, n, m_l, m_s\}$, with \mathbf{r}_j representing atomic positions and n, l, m_l, m_s denoting atomic quantum numbers. In the context of QGT, the key quantities are the wave-function gradients in reciprocal space, highlighting the necessity of determining the coefficients $C_j(\mathbf{k})$ across the entire reciprocal space. A central aspect of our study is resolving how to extract the magnetic quantum number m_l , synonymous with OAM, from CD-ARPES maps.

Here, we analyze in detail the physics underlying the CD-ARPES process by comparing experimental maps to respective theoretical calculations. For our study we focus primarily on two technologically important materials, graphene and WSe₂, while spectra from a kagome magnet GdMn₆Sn₆ and a topological metal PtTe₂ are also presented.

We qualitatively explain CD-ARPES maps from graphene by coherently adding multiply scattered atomiclike emissions, calculated within a real-space photoelectron diffraction formalism [26] and taking into account the two nonequivalent atomic sites. These results are compared to one-step model calculations based on the Korringa-Kohn-Rostoker formalism [27]. Subsequently, a similar analysis is discussed for WSe₂, a material that exhibits a dominant W 5d $Y_2^{\pm 2}$ orbital character at the K and K' points in the Brillouin zone. Recall that the results of one-step model calculations for graphene and WSe₂ were previously published in Refs. [27–31].

During the photoemission process with circularly polarized light, electrons can acquire nonzero OAM through dipole selection rules, regardless of their initial state OAM. This leads to OAM-dependent scattering processes, known as the Daimon effect [32], and moreover it can lead to large CD-ARPES signals even in the absence of the initial-state OAM. In case of graphene, we demonstrate the mutual impact of these processes on the experimental CD-ARPES maps. Concerning WSe₂, a further modulation of the signal related to spin-orbit coupling (SOC) is analyzed. To broaden our analysis, we also explore the CD-ARPES signals from GdMn₆Sn₆ and PtTe₂, highlighting several important features that showcase the versatility of CD-ARPES across different materials. By establishing the framework outlined, our work not only sets a benchmark for interpreting both past and future dichroic photoemission experiments, but also opens the door to extracting transport-relevant information from CD-ARPES data.

II. RESULTS

Figure 1 shows exemplary experimental CD-ARPES maps from graphene and WSe₂ (additional maps are shown in the Supplemental Material [33]). The Dirac states at the K and K' points of graphene are made up almost exclusively of C $2p Y_1^0$ (that is $2p_z$) orbitals that carry zero OAM. Therefore, if CD-ARPES was to mirror their OAM character, the dichroic signal from the Dirac states of graphene should vanish. Instead, the maps in Figs. 1(b)–1(d) exhibit strong and rich dichroic signals, which vary significantly with energy. As discussed in the Supplemental Material [33], CD-ARPES maps from graphite closely resemble results obtained from graphene, suggesting that the substrate does not significantly impact the overall character of the maps.

In close vicinity of the K and K' points, the topmost valence bands of WSe₂ are primarily of W 5d $Y_2^{\pm 2}$ character, that is, they carry OAM of $\pm 2\hbar$. If CD-ARPES was to be sensitive to the OAM, the maps should exhibit sign inversion between K and K' points. Instead, the map in Fig. 1(g) displays a complex pattern of sign reversals, not clearly alternating between K and K' points. In order to explain this behavior qualitatively, we employ a photoemission model based on the tight-binding formalism for the ground-state band structure and atomiclike photoionization profiles [34]. The latter are augmented with multiple scattering in a real-space cluster [26,35]. For a two-dimensional (2D) solid, the model is based on the coherent addition of photoelectron emissions originating from participating Y_l^m orbitals of the nonequivalent sites in the unit cell.

In the case of graphene, there are two nonequivalent sites, labeled A and B in this paper. For the Dirac π bands [36] each one contributes with a single Y_1^0 orbital. In the first level of approximation, that is, the independent atomic center approximation (IACA) [29], atomiclike photoionization profiles M_A and M_B due to emitters A and B are combined coherently. This is done taking into account parallel momentum conservation, phases of momentum-dependent complex coefficients from the tight-binding model of graphene with nearest-neighbor hopping [36,37], as well as phase shifts due to positions of emitters with respect to the emission direction. The initial-state tight-binding wave function of graphene can be written as $\psi(\mathbf{k}) = A(\mathbf{k}_{\parallel})|C_A\rangle + B(\mathbf{k}_{\parallel})|C_B\rangle$, where $|C_A\rangle$ and $|C_B\rangle$ are

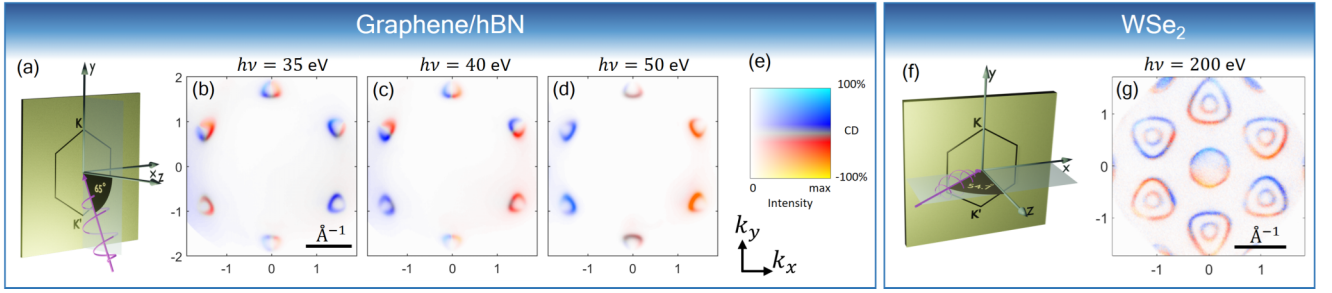


FIG. 1. Experimental CD-ARPES from a monolayer of graphene on hBN (a)–(e) and for WSe₂ (f), (g). (a) Experimental setup for graphene, the light is incident at $\theta_{h\nu} = 65^\circ$ off-normal. (b)–(d) CD-ARPES maps for $h\nu = 35, 40,$ and 50 eV, respectively, constant energy cuts are at the binding energy $E_B = 1.25$ eV. (f), (g) Experimental setup and the CD-ARPES map for WSe₂ taken at $h\nu = 200$ eV and $\theta_{h\nu} = 54.7^\circ$. The constant energy cut in (g) is at 0.725 eV below the valence band maximum at K/K' points (see Supplemental Material [33] for details). Panels (b)–(d) and (g) are centered at normal emission and use the color scale shown in (e). In both setups, (a) and (f), the reaction plane coincides with a mirror plane of the surface, which is reflected in the CD-ARPES maps by the sign reversal upon reflection at the mirror plane.

atomic $C 2p Y_1^0$ wave functions centered on the two nonequivalent sites within the unit cell and $A(\mathbf{k}_{\parallel})$ as well as $B(\mathbf{k}_{\parallel})$ are complex coefficients. The total transition matrix element then reads as

$$M_{fi}(\mathbf{k}_f) \propto [A(\mathbf{k}_{\parallel}) \cdot M_A(\mathbf{k}_f) + B(\mathbf{k}_{\parallel}) \cdot M_B(\mathbf{k}_f)] \times \delta(h\nu - E_k - W - E_B), \quad (2)$$

where E_B is the binding energy, W the work function, and \mathbf{k}_f the wave vector of the detected far-field photoelectron.

For normal light incidence, $\theta_{h\nu} = 0^\circ$, dipole selection rules require $Y_1^0 \rightarrow Y_2^{\pm 1}$ for C_{\pm} light, and CDAD vanishes (see Supplemental Material [33] for details). For our experimental geometry with off-normal light incidence at $\theta_{h\nu} = 65^\circ$ the matrix elements $M_{A,B}$ calculated by EDAC code [26] and the resulting CDAD are shown in Figs. 2(a)–2(e). The intensity profiles in Figs. 2(a) and 2(b) depend on the light chirality and, despite $m = 0$, lead to nonvanishing CDAD patterns shown in Figs. 2(c) and 2(e), a result known from atomic physics [22].

The results for graphene according to Eq. (2), using atomic photoionization patterns and phases of the nearest-neighbor tight-binding model coefficients, are shown in Figs. 2(f) and 2(g) for $\theta_{h\nu} = 0^\circ$ and in 2(h) and 2(i) for $\theta_{h\nu} = 65^\circ$. It

is instructive not only to inspect the calculated ARPES maps, Figs. 2(f) and 2(h), but also maps in which the $\delta(h\nu - E_k - W - E_B)$ term was not taken into account; the latter could be imagined as approximately visualizing CD-ARPES over the entire π band, as explained in Fig. 2(j) (rigorously, this neglects that different momentum regions of the π band are probed at different kinetic energies). Figures 2(g) and 2(i) exhibit dark corridors, that is, regions of vanishing or at least small intensity. These result from the blue regions in Fig. 2(k), that is, regions of phase difference of π between $A(\mathbf{k}_{\parallel})$ and $B(\mathbf{k}_{\parallel})$ [27,37,38]; then emissions from sites A and B enter with opposite signs. The dark corridor emerges for emission directions where, within IACA, nonequivalent sites contribute with the same intensity, as is the case for the plane shown in Fig. 2(l), and therefore is strictly valid within Eq. (2).

Figures 2(h) and 2(i) show predicted CD-ARPES according to Eq. (2). Figure 2(i) is an intensity-modulated atomic pattern of Fig. 2(c) and demonstrates that the linear combinations of atomlike photoionization patterns, Eq. (2), cannot explain the experimental patterns of Figs. 1(b)–1(d) that exhibit additional intracontour CD sign reversals.

In the following we will extend Eq. (2) by including photoelectron scattering. Conceptually, this is done in

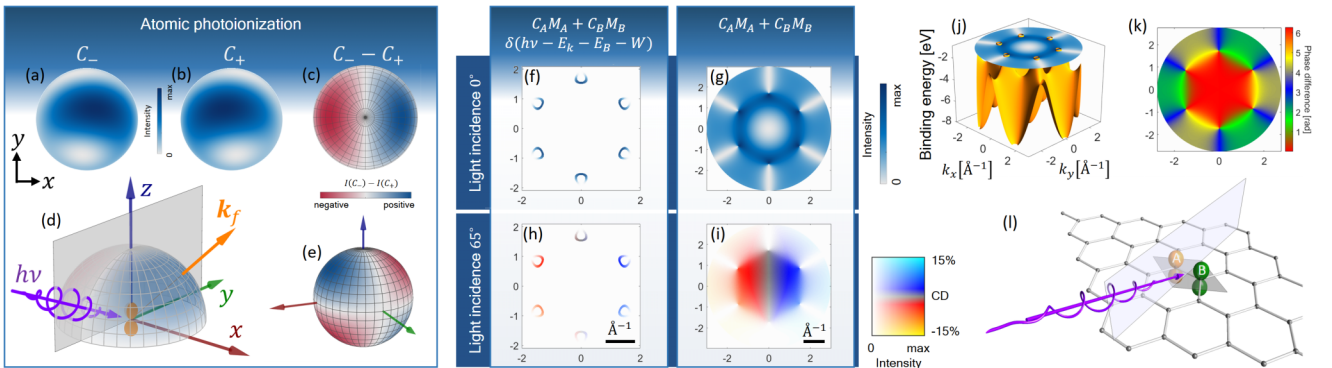


FIG. 2. (a)–(e) CDAD from a $C 2p Y_1^0$ orbital at $\theta_{h\nu} = 65^\circ$ and $h\nu = 40$ eV calculated using EDAC code [26]. (f), (g) Theoretical photoemission from graphene according to Eq. (2) at $\theta_{h\nu} = 0^\circ$, $h\nu = 40$ eV, and $E_B = 1$ eV with (f) and without (g) energy conservation (confer text). The band structure is depicted in (j). (h), (i) As in (f) and (g), but at $\theta_{h\nu} = 65^\circ$. A special 2D color map visualizes simultaneously CD and intensity. (k) Difference between complex phases of the coefficients $A(\mathbf{k}_{\parallel})$ and $B(\mathbf{k}_{\parallel})$ of graphene π bands in the tight-binding model. (l) Graphene lattice with nonequivalent sites A and B ; the gray rhombus indicates the unit cell, and the rectangle indicates the photoemission reaction plane with light incident at $\theta_{h\nu} = 65^\circ$.

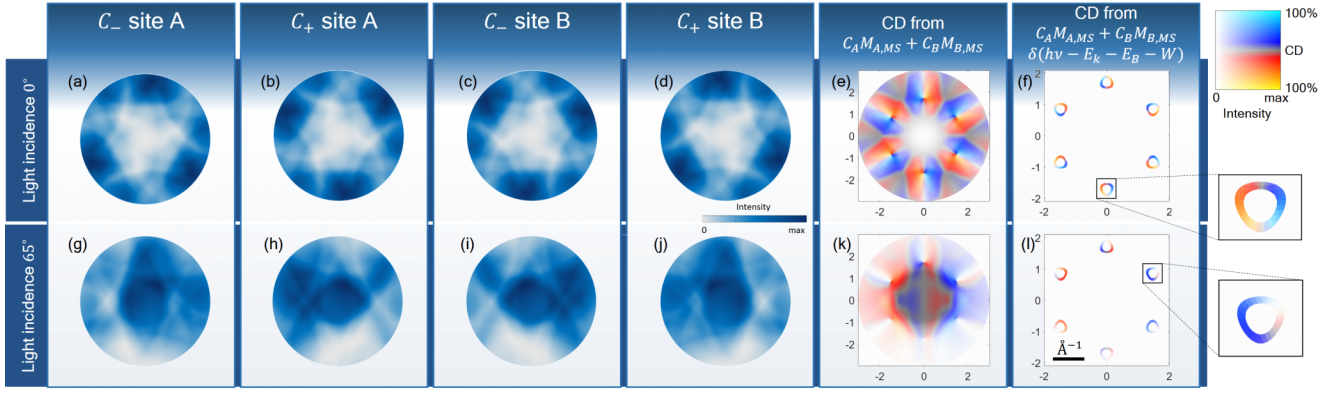


FIG. 3. (a)–(d) Photoelectron diffraction patterns at $\theta_{hv} = 0^\circ$ and $h\nu = 40$ eV over the upper half-space [compare Fig. 1(d)] for the graphene sites A and B excited with C_\pm radiation, as indicated. Patterns (a)–(d) are added coherently, taking into account amplitudes, phases, interatomic interferences, as well as the coefficients $A(\mathbf{k}_\parallel)$ and $B(\mathbf{k}_\parallel)$ without (e) and with (f) energy conservation $\delta(h\nu - E_k - W - E_B)$. (g)–(l) Same as (a)–(f) but at $\theta_{hv} = 65^\circ$. The complex phases related to (a)–(d) and (g)–(j) are shown in the Supplemental Material [33].

a straightforward way by replacing atomiclike matrix elements $M(\mathbf{k}_f)$ by their multiple scattered (MS) counterparts $M_{MS}(\mathbf{k}_f)$. In this approach a cluster of atoms around the emitter site is considered, the scattered wave originating from the emitter site is calculated and used as a final state in $M_{MS}(\mathbf{k}_f)$ [26,35,39]. Both elastic and inelastic processes can be taken into account, the latter ones by including a finite inelastic mean-free path (IMFP). This type of calculation is performed within the photoelectron diffraction formalism [29,40,41], here using EDAC [26]. The results are shown in Fig. 3, with Figs. 3(a)–3(f) related to $\theta_{hv} = 0^\circ$ and 3(g)–3(l) to $\theta_{hv} = 65^\circ$.

Let us first focus on $\theta_{hv} = 0^\circ$. Figures 3(a)–3(d) show $|M_{A,MS}(\mathbf{k}_f)|^2$ and $|M_{B,MS}(\mathbf{k}_f)|^2$ for C_\pm excitations, over the half-space above the surface [see Fig. 2(d)]. These patterns differ significantly from the dipole-allowed atomic $|Y_2^{\pm 1}|^2$ patterns (see Supplemental Material [33]), and their symmetries reflect the trigonal environment of nearest neighbors, together with the intensity modulations due to the Daimon effect [32]. The patterns are chiral, for each site the chirality is reversed upon reversing the light helicity. Furthermore, patterns are connected by various mirror reflections related to the fact that a mirror reflection through any plane parallel to z reverses the light helicity, and to the glide reflections that connect local environments of sites A and B (lattice translations do not influence far-field intensity patterns), for example (a) becomes (b) upon \mathcal{M}_y and (a) becomes (d) upon \mathcal{M}_x .

The results of coherently combining the patterns of Figs. 3(a)–3(d) are shown in 3(e) and 3(f), without and with taking into account the energy conservation $\delta(h\nu - E_k - W - E_B)$ [similarly to Figs. 2(f) and 2(g)]. Since at $\theta_{hv} = 0^\circ$, atomiclike CDAD vanishes, the CD-ARPES pattern in Fig. 3(f) stems exclusively from final-state scattering, that is a variant of the Daimon effect [32] for valence electrons. The magnitude of the CD asymmetry

$$\frac{|M_{fi,MS,C_-}|^2 - |M_{fi,MS,C_+}|^2}{|M_{fi,MS,C_-}|^2 + |M_{fi,MS,C_+}|^2} \quad (3)$$

reaches $\approx 80\%$.

Figures 3(g)–3(j) show angular intensity patterns for $\theta_{hv} = 65^\circ$. Compared to Figs. 3(a)–3(d) some symmetries are missing, with the remaining \mathcal{M}_x mirror operation that connects Figs. 3(h) with 3(j) and 3(h) with 3(i), as expected from the reversal of light helicity together with glide mirror transformation swapping sites A and B. Importantly, the patterns differ qualitatively from the atomiclike patterns of Figs. 2(a) and 2(b). The CD-ARPES pattern in Fig. 3(k) exhibits similarities to the IACA pattern in Fig. 2(c), but only concerning the intensity, the CD pattern is qualitatively different. The magnitude of the CD again reaches about 80%. The dark corridor is strict (zero signal) neither in Fig. 3(e) nor in 3(k), in agreement with one-step model calculations [27]. Along the $k_x = 0$ momentum trajectory the intensity reaches $\approx 5\%$ of the maximum intensity. In order to validate the findings of our real-space scattering model, we compare the experimental CD-ARPES maps taken at $h\nu = 35, 40,$ and 50 eV shown in Figs. 1(b)–1(d) with respective results from one-step model photoemission calculations shown in Figs. 4(a)–4(c), performed with the previously used setup [27]. In this energy range, the sign of the experimental CD behaves differently for different Dirac contours, which we label D1–D6 [cf. Fig. 4(a)]. The experimental behavior is partly reproduced in the one-step model calculations, for example, the reversal of the CD sign between $h\nu = 35$ and 50 eV for contours D2 and D3. Also the sign change of the intracontour CD is reproduced for D4–D6 [Figs. 1(c) and 4(b)], as is the weakening of intracontour sign flip for D1 and D6 in Figs. 1(d) and 4(c). On the other hand, the sign of contours D2 and D3 is not correctly reproduced [Figs. 1(c) and 4(b)].

So far we discussed the physics of nonvanishing CD-ARPES in graphene, a material in which initial states carry negligible OAM and spin polarization. In the following we will extend the discussion to WSe_2 , in which the initial states carry orbital and spin polarization. In WSe_2 near the K/K' points, the states at the valence band maximum are primarily of $W 5d Y_2^{\pm 2}$ character with an additional spin-polarized splitting [42]. As discussed in the Supplemental Material [33], the admixture of other orbitals near K/K' is not negligible, nevertheless, in the following we will focus on dominant contributions by $W 5d Y_2^{\pm 2}$.

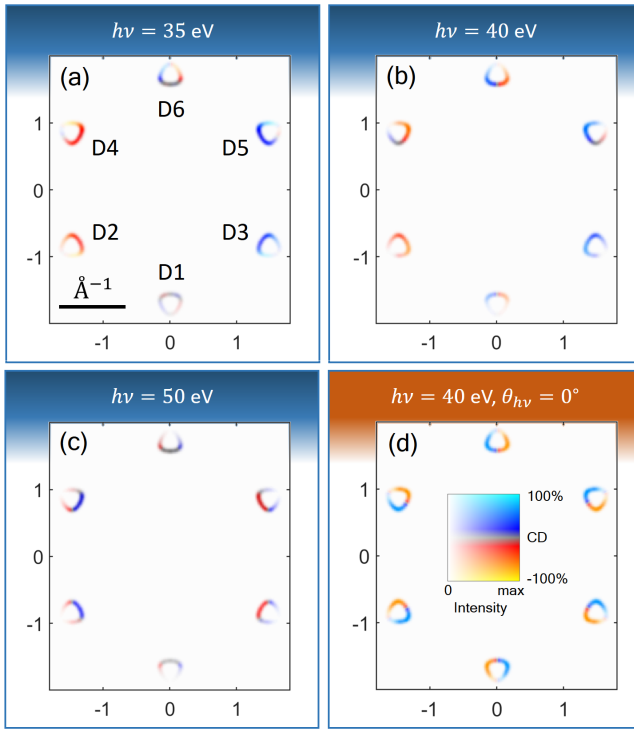


FIG. 4. Theoretical photoemission calculated within the one-step model for graphene at $E_B = 0.8$ eV and $\theta_{h\nu} = 65^\circ$: (a) $h\nu = 35$ eV, (b) 40 eV, and (c) 50 eV. (d) Same as (b) but at $\theta_{h\nu} = 0^\circ$. The color map used in all panels is shown in (d), all scales are in \AA^{-1} .

Figure 5 shows theoretical photoelectron diffraction results at $h\nu = 200$ eV from a W $5d Y_2^{\pm 2}$ orbital in the surface layer of bulk WSe₂ [Fig. 5(a); the coordinate system is defined in Fig. 5(b)]. The atomiclike CDAD profiles from Y_2^2 and

Y_2^{-2} exhibit sign reversals, as shown in Figs. 5(c) and 5(d), respectively. This indicates that already within IACA different CD signs can be expected for different emission angles [43], and there may exist regions where the CDAD vanishes. On the other hand, the positions of these sign changes vary slowly with emission angle, and, as shown in Fig. 5(e), the entire first BZ encloses the same sign of atomic CDAD near normal emission at $h\nu = 200$ eV. This demonstrates that rapid CD sign changes [see Fig. 1(g)] in the vicinity of a K or K' point are unlikely to originate from atomiclike CDAD patterns, even if one considers coherent summation of such patterns from all sites in the spirit of Eq. (2). Figure 5(f) shows the pattern of emission over the full sphere, which, when angle integrated, will yield a net CD signal. This reflects a net sensitivity of angle-integrating methods based on core-level absorption to the OAM. However, in such methods typically only the $l + 1$ channel is significant (e.g., $2p$ to $3d$ channel in transition metals), and the three-step model description is sufficient (we discuss this further in the Supplemental Material [33]).

Figures 5(g) and 5(h) show the photoelectron diffraction maps for $Y_2^{\pm 2}$ orbitals with multiple scattering included. Figures 5(i) and 5(j) show portions of the same maps, converted to the momentum scale and with overlaid theoretical contours. These results qualitatively explain rapid variations of the CD-ARPES signal from WSe₂ as being due to multiple scattering.

With the quantization axis along the surface normal, the CDAD vanishes for orbitals with $m = 0$ for normal light incidence, potentially simplifying the interpretation of CD-ARPES maps. Figures 6(a) and 6(b) show CD-ARPES results from WSe₂ at normal light incidence and $h\nu = 60$ eV from the terraces A and B , as shown in Fig. 6(c). In these experiments, the angle between the incoming light and normal emission is fixed at 54.7° , therefore, the maps in Figs. 6(a) and 6(b) are probing a momentum section between the second and third

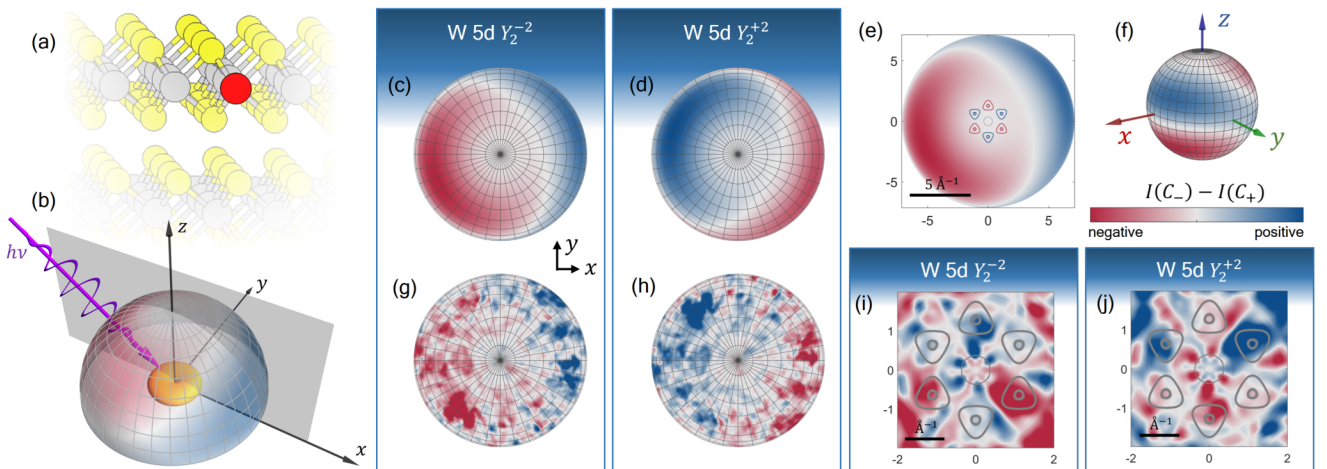


FIG. 5. Photoelectron diffraction from W $5d Y_2^{\pm 2}$ orbitals in WSe₂ at $h\nu = 200$ eV calculated using EDAC [26]. (a) Outermost layers of WSe₂ with an emitter W atom indicated in red. (b) Experimental geometry with the reaction plane (gray rectangle) and the 10° step grid in polar and azimuthal angles; the orange contour represents a $Y_2^{\pm 2}$ orbital. (c), (d) CDAD signal from W $5d Y_2^{-2}$ and Y_2^{+2} orbitals, respectively. (e) Same as (c), but converted to the momentum scale and with overlaid theoretical contours at $E_{\text{VBM}} - 0.5$ eV for bulk WSe₂. The contours at the three K points are related to the Y_2^2 map, while those at the K' points would be related to the Y_2^{-2} map. Such alternation of the CD sign would provide OAM sensitivity under IACA (our assignment of K/K' is arbitrary). (f) Same as (c), but for emission angles over the full sphere. (g), (h) Same as (c) and (d), but with multiple scattering included. (i), (j) Same as (g) and (h), but converted to the momentum scale and with theoretical contours as in (e). Maps for other kinetic energies are shown in the Supplemental Material [33].

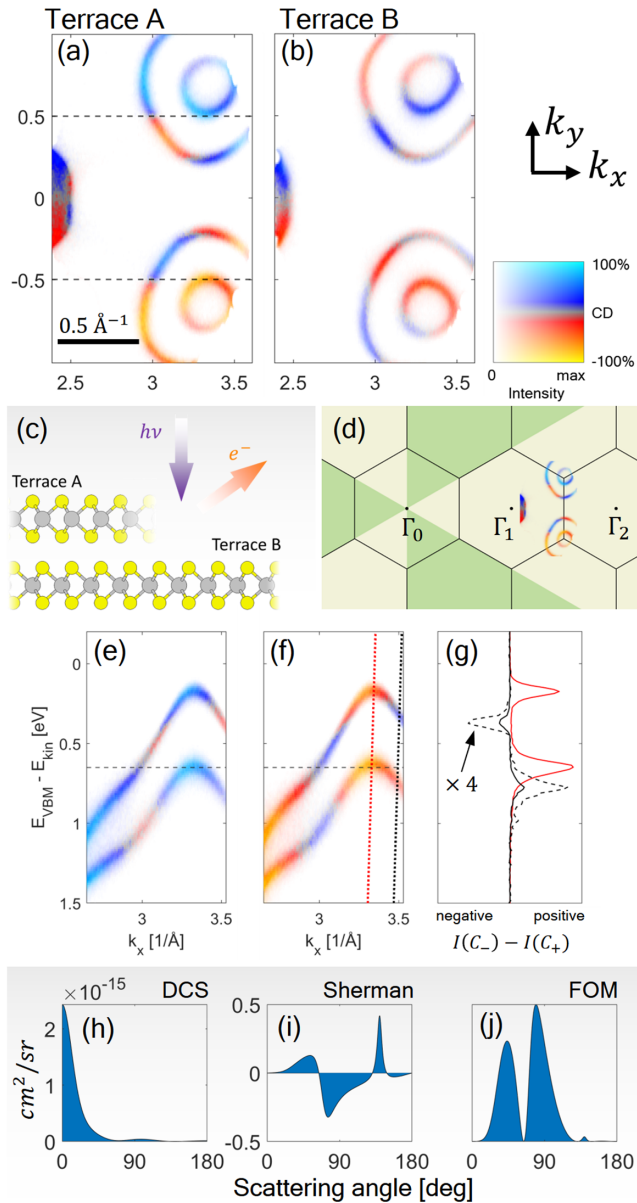


FIG. 6. Photoemission from WSe₂. (a), (b) Constant-energy cuts at $E_{\text{VBM}} - E_{\text{kin}} = 0.64$ eV for terraces A and B at $h\nu = 60$ eV and $\theta_{h\nu} = 0^\circ$ as indicated in (c). E_{VBM} refers to the valence band maximum at the K/K' points, the assignment of terraces in (c) is arbitrary. (d) Position of (a) in momentum space. (e), (f) Energy-momentum cuts along the dashed lines in (a). The horizontal dashed line indicates the energy in (a) and (b). (g) Red and black solid curves show the intensity difference $I(C_-) - I(C_+)$ along red and black dotted lines in (f). The dashed black line is multiplied by a factor of 4. (h) Differential cross section (DCS) for scattering of free electrons at W atoms, calculated using ELSEPA [44] with Sherman function S (i) and figure-of-merit $\text{DCS} \times S^2$ (j) [45].

BZ, as shown in Fig. 6(d). Since the K and K' points are swapped at subsequent terraces [42,46], any swapping of the CD sign between K and K' in maps in Figs. 6(a) and 6(b) can be potentially related to the initial-state OAM. Indeed such CD sign reversals are present, however, only along sections of the K and K' contours. Inner contours exhibit constant CD

sign in Fig. 6(a) while the intracontour sign reversal is present in Fig. 6(b). The difference between Figs. 6(a) and 6(b) is due to the final-state scattering combined with the atomic final-state profile because terraces A and B have reversed polarities along the x axis, which causes a difference in scattering. This effectively divides the CD-ARPES maps into nonequivalent regions, as indicated by beige and green segments in Fig. 6(d).

Figures 6(e) and 6(f) show energy-momentum cuts along the dashed lines in Fig. 6(a) that are in the vicinities of K/K' points. At some momenta the CD sign of the two split bands is opposite, as shown by black curves in Fig. 6(g). Since within a layer these states carry the same OAM but opposite spin polarization [42,46] (see the Supplemental Material [33] for details), this finding can be related to spin-orbit scattering in the final state [45,47]. To estimate this effect, it is useful to study differential cross section and the Sherman function of W atoms, both shown in Figs. 6(h) and 6(i) together with their figure-of-merit (FOM) in Fig. 6(j) [45,48]. Indeed, at $E_{\text{kin}} = 60$ eV, a W atom is expected to produce significant spin polarization at scattering angles between 30° and 100° . When considering various W and Se emitters and nearest-neighbor and next-nearest-neighbor scatterers, this may lead to the spin-dependent inversions of the CD sign shown in Figs. 6(f) and 6(g).

Figure 7 shows CD-ARPES energy-momentum maps for two additional materials, a kagome magnet GdMn₆Sn₆, where electron correlations play a role [49], and a topological metal PtTe₂ that can be described by one-electron physics [50–52].

GdMn₆Sn₆ data have been measured in the experimental geometry indicated in Fig. 7(a), where the reaction plane overlaps with one of the sample mirror planes. Through the axial vector mirror reflection rules, this implies that CD-ARPES maps are odd in k_y , as indeed exemplified in Figs. 7(b)–7(d). Importantly, all three panels exhibit dominating CD sign at negative and positive k_y , with local CD sign reversals only observed in Fig. 7(c) and only for the quasiparticle bands near the Fermi level. For $E_B > 0.6$ eV, correlated electrons exhibit a simple CD pattern, with no CD sign reversals on either side of $k_y = 0$. This suggests that the observed behavior might be primarily due to the IMFP-derived CD, as discussed by Moser [53].

The CD-ARPES maps from PtTe₂ were measured in two geometries. In the geometry of Fig. 7(f), the reaction plane coincides with the mirror plane of the sample, and therefore the CD maps in Figs. 7(g)–7(j) are odd in k_y . We present the maps in two ways; Figs. 7(g) and 7(h) are plotted using the 2D color map of Fig. 7(e), while in Figs. 7(i) and 7(j) only the absolute CD signal is plotted, according to the color map in Fig. 7(l). PtTe₂ exhibits a surface Dirac cone centered at $\bar{\Gamma}$ at E_B between 2 and 3 eV [50–52], as indicated in box 1 in Fig. 7(h). This Dirac cone is expected to exhibit spin-momentum locking, which leads to the two branches having opposite spin polarization. It has been shown that for topological insulators CD-ARPES can potentially be a probe of this spin-momentum locking [6,54], however, this behavior is not observed in our experiments, where, e.g. for positive k_y , both upper and lower branches of the Dirac cone exhibit the same CD sign.

By comparing Figs. 7(g) and 7(h) with 7(i) and 7(j) we demonstrate that nonvanishing CD signal is present also in

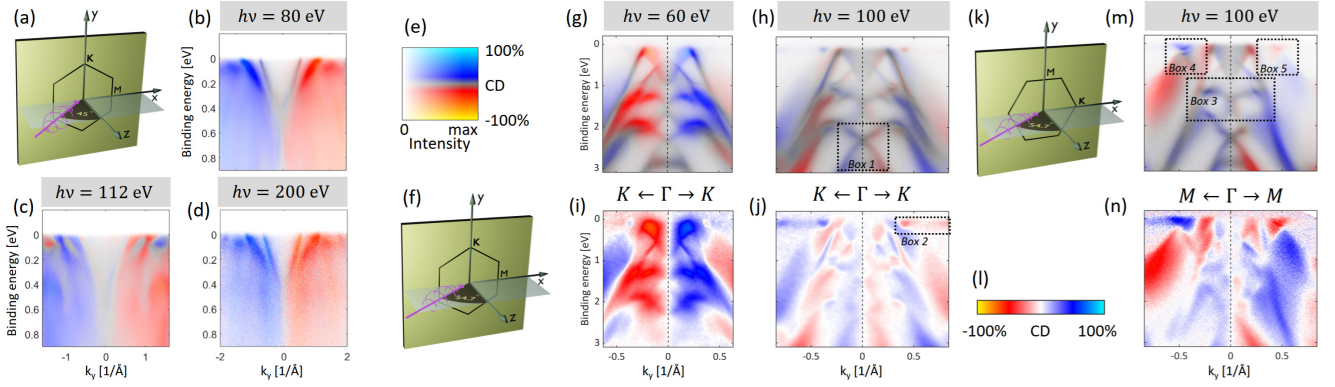


FIG. 7. (a)–(d) Experimental geometry and CD-ARPES energy-momentum maps from GdMn_6Sn_6 along ΓK reciprocal direction at $h\nu = 80$ eV (b), $h\nu = 112$ eV (c), and $h\nu = 200$ eV (d). Panels are plotted using the 2D color map shown in (e). (f)–(n) Experimental geometries and CD-ARPES energy-momentum maps from PtTe_2 . Experimental geometry in (f) refers to (g)–(j), while the geometry in (k) to panels (m) and (n). (g), (i) Taken at $h\nu = 60$ eV, while (h), (j), (m), and (n) were taken at $h\nu = 100$ eV. Upper panels (g), (h), and (m) are plotted using the 2D color map shown in (e), while lower panels (i), (j), and (n) show CD magnitude according to the color map shown in (l). Spectra taken at ≈ 40 K. Features indicated by boxes 1 to 5 in (h), (j), and (m) are discussed in the text.

the regions of the expected projected band structure gaps. As exemplarily indicated in Fig. 7(j) by box 2, a resulting flat CD-ARPES band appears at the Fermi level, where inelastic scattering is expected to play a minor role.

In the geometry of Fig. 7(k) mirror planes of the crystal are broken by the experimental geometry ($\Gamma - K$ is not a mirror plane of PtTe_2) and therefore CD-ARPES maps in Figs. 7(m) and 7(n) are not symmetric in k_y , as indicated for example by box 3 in 7(m) where both the CD sign and the energy positions of bands are asymmetric for $\pm k_y$. These asymmetries stem primarily from interatomic interferences [55] and asymmetric multiple scattering. In addition, the trigonal symmetry of the bulk band structure, in connection with approximate k_\perp sensitivity of ARPES, may also play a role.

Projected band structure is made from overlapping allowed continuous regions in energy-momentum maps that often originate primarily from one type of orbital [56], therefore, such different regions can be expected to have different responses in CD. Boxes 4 and 5 in Fig. 7(m) illustrate the regions where such sensitivity appears to take place, with the electron pockets that host surface state [51] having opposite CD sign to the surrounding projected bands [the same applies to the tiny electron pockets in Fig. 7(h)]. However, it remains to be established under which conditions this contrast can be considered as a faithful representation of the initial state band character.

III. DISCUSSION

Within the tight-binding formalism, the photoemission signal is a coherent sum of emissions originating from various orbitals that form the valence band structure. As a result, it carries information not only about the contributing orbitals but also about their relative phases, encoded in the complex coefficients $C_j(\mathbf{k})$ of Eq. (1), momentum gradients of which can serve as crucial inputs for the QGT [23]. A striking manifestation of such phase interference is the dark corridor in graphene [27]. However, in the case of CD-ARPES, the situation is more delicate, as it involves analyzing differences between signals rather than absolute intensities.

Our results for graphene show that through the Daimon effect [32] strong CD-ARPES is present even in the absence of SOC. Therefore, in materials in which SOC is relevant, the challenge is in isolating the initial-state OAM from other contributing effects. For a material of the WSe_2 family, where bands with $m = \pm 2$ alternate between the K and K' points, the breaking of the intralayer inversion symmetry that splits the $m = \pm 2$ derived bands is also responsible for asymmetries in the CD photoelectron diffraction maps. These asymmetries originate not only from the final-state scattering, but also from interatomic interferences, with the phase shift $\exp[i\mathbf{k}_f \cdot (\mathbf{r}_A - \mathbf{r}_B)]$ already present in the free-electron final-state approximation, and are relevant for systems with band characters mixed between two of more different sites within the unit cell [55]. These modifications of amplitudes and phases appear on top of C_j coefficients of Eq. (1). As a result, without the knowledge of the multiply scattered matrix elements from contributing orbitals, no linear combination of dichroic signals taken at different geometries can *a priori* isolate contributions from the initial-state OAM from those related to interatomic interference and multiple scattering,

Without prior knowledge of the material, identifying that the patterns in Figs. 1(b)–1(d) originate from $m = 0$ orbitals can be challenging. These patterns illustrate the complexity of the photoemission process, where not only multiple scattering but also accurate modeling of the surface barrier and the optical potential [57,58] may be crucial. Further progress can be made by augmenting present state-of-the-art one-step model computer codes with a full-potential approach [59] instead of relying on the muffin-tin approximation.

Since CD-ARPES is a technique at least an order of magnitude faster compared to spin-polarized ARPES, for it does not require a special detector system, probing spin polarization using CD-ARPES has been long sought [6]. Figures 6(f) and 6(g) suggest how spin sensitivity of CD-ARPES can be achieved through spin-orbit scattering in the final state at tungsten (high-Z) atoms. A possible scenario is that CDAD and the Daimon effect vanish at a certain \mathbf{k}_f , allowing SOC scattering to be observed. Indeed the CD sign reversal in Ref. 6(g) appears in a region in which the net CD signal is small. However,

to confirm these conjectures further numerical calculations are necessary in order to eliminate effects due to small differences in orbital contributions between the two split bands near the K/K' points.

Despite the described complexities, we conjecture that there might exist regimes where the contributions from initial-state OAM, interatomic interferences, and multiple scattering can be disentangled. One such regime could occur when the influence of multiple scattering acts as a slowly varying background, as expected at very low kinetic energies, where a forward scattering peak is broad and thus may lead to suppression of the Daimon effect. Such scenario also needs to involve a rapidly varying OAM in the reciprocal space, and it might be realized when measuring topological surface states using a 6-eV laser [6,60]. In the latter case, disentangling contributing C_j coefficients [Eq. (1)] would primarily involve interatomic interferences of the atomic matrix elements $M(\mathbf{k}_f)$. A further promising regime might also emerge at very high energies, although its applications could be constrained by limited energy resolution.

In Fig. 7, we demonstrate that the complexity and rich physics of CD-ARPES are not confined to specific materials but rather open new avenues for studying the electronic structure of quantum materials. Future extensions of our work may include investigating spin-dependent electron transmission through ultrathin layers, exploring the OAM and spin polarization of hot electrons following excitation by ultrashort laser pulses [19], and developing schemes to generate OAM electron beams via photoemission [61]. Furthermore, the photoemission matrix element acts on the entire electron charge, making it reasonable to assume that CD-ARPES captures the quantities described by the modern theory of polarization [62], rather than being limited to the atomic contributions expressed in the tight-binding model of Eq. (1). The distinction between these contributions has been a subject of debate even in the simpler case of x-ray magnetic circular dichroism [63–65], highlighting an intriguing direction for future research.

IV. METHODS

A. ARPES based on photoelectron diffraction

With the tight-binding (LCAO) initial wave function $\psi_i = \sum_{l,m,\mathbf{r}_j} C_{l,m,\mathbf{r}_j} \phi_{l,m,\mathbf{r}_j}$, the dipole matrix element for optical transition reads as

$$M_{fi}(\mathbf{k}_f) \propto \langle \psi_f | \mathbf{A} \cdot \mathbf{p} | \sum_{l,m,\mathbf{r}_j} C_{l,m,\mathbf{r}_j} \phi_{l,m,\mathbf{r}_j} \rangle \times \delta(h\nu - E_k - W - E_B), \quad (4)$$

where ϕ are atomic wave functions at all sites \mathbf{r}_j and for all participating quantum numbers l, m ; C are complex coefficients. The matrix element may be rewritten as

$$M_{fi}(\mathbf{k}_f) \propto \sum_{l,m,\mathbf{r}_j} C_{l,m,\mathbf{r}_j} \cdot \langle \psi_f | \mathbf{A} \cdot \mathbf{p} | \phi_{l,m,\mathbf{r}_j} \rangle \times \delta(h\nu - E_k - W - E_B). \quad (5)$$

Let us define $M_{l,m,\mathbf{r}_j}(\mathbf{k}_f) = \langle \psi_f | \mathbf{A} \cdot \mathbf{p} | \phi_{l,m,\mathbf{r}_j} \rangle$. In photoelectron diffraction codes the dipole operator $\mathbf{A} \cdot \mathbf{p}$ is often

replaced by the length form $\boldsymbol{\varepsilon} \cdot \mathbf{r}$ [26], which is appropriate because of the localized nature of ϕ . The key difficulty in evaluating $M_{l,m,\mathbf{r}_j}(\mathbf{k}_f)$ is in finding the ψ_f . An advantage of photoelectron diffraction codes is that ψ_f is effectively spatially limited to the region surrounding ϕ_{l,m,\mathbf{r}_j} , exploiting the inelastic mean-free path and a decay of spherical waves with the distance from the emitter ϕ_{l,m,\mathbf{r}_j} .

The final state ψ_f is the time-reversed low-energy electron diffraction (LEED) state, therefore, it is a sum of outgoing plane waves $e^{i\mathbf{k}_f \cdot \mathbf{r}}$ and spherical waves incoming into each site [66,67]. A LEED state is a sum of incoming plane-wave $e^{-i\mathbf{k}_f \cdot \mathbf{r}}$ and spherical waves outgoing from each site. With muffin-tin potentials, the IACA approximation corresponds to neglecting a contribution of spherical waves, either emitted or reflected from neighboring sites, to the final state at the considered site, and as a consequence also neglecting any multiple scattering.

In case of the EDAC code [26] it is preferred that $\phi_{l,m,\mathbf{r}}$ is contained within its muffin-tin (MT) sphere. According to our WIEN2K calculations [68] for nearly touching MT spheres of C $2p$ in graphene, only 39% of the charge is within a MT sphere. In WSe₂ $\approx 72\%$ of the charge of W $5d$ and 59% of the charge of Se $4p$ orbitals is within their MTs. This charge leakage out of MT spheres and overlap with neighboring MTs is affecting the evaluation of spherical wave function due to the emitter [26,67]; however, this might not be critical since in general intensities of photoelectron diffraction (PED) patterns are known to reflect atomic photoionization profiles, and large scattering contributions observed in CD-ARPES occur because they reflect intensity differences (between patterns taken with C_{\pm} light). At least for the graphene π bands, the leaking effect might be somewhat minimized because the C $2p$ Y_1^0 orbitals primarily extend out of plane, where there are no nearest-neighbor MTs. To mitigate some of these issues, Krüger [66] used the acceleration form of the dipole matrix element.

Furthermore, one may consider that the photoemission process creates a localized Coulomb hole within the electron gas [69,70], and that the final state is represented by a partial wave expansion of the free (scattering) states of this potential. However, such effects can often be neglected, especially in metals where the photohole is screened. EDAC code [26] accounts for this effect by adding a screened photohole to the MT potential of the emitter.

Since for a periodic solid the photoemission signal derived from Eq. (5) has a form of a Bloch sum, the parallel-momentum conservation $\mathbf{k}_{f\parallel} = \mathbf{k}_{i\parallel}$ is obeyed and the sum in Eq. (5) can be limited to orbitals within a unit cell only, when using momentum-dependent coefficients $C_{l,m,\mathbf{r}_j}(\mathbf{k}_{i\parallel})$. A more detailed discussion on this and related issues in the context of modern PED is presented for instance in Refs. [34,35,39].

Because of the coherent propagation, our approach can be considered as a one-step model. Key approximations are related to the LCAO wave function, muffin-tin potentials (in contrast to more precise full-potential methods), and to the charge leaking out of the MT spheres. Furthermore, in EDAC the surface barrier is approximated by a potential step, while more accurate modeling is known to affect the results considerably [57,58].

B. Tight-binding model for the π bands of graphene

Graphene is a single honeycomb layer of carbon atoms. In its unit cell, there are two carbon atoms C_A and C_B separated by $a_{CC} \approx 1.42$ Å. Bands that form Dirac cones of graphene are primarily made (>97% contribution, according to our WIEN2K [68] calculations) of C $2p_z$ orbitals. The nearest-neighbor hopping Hamiltonian for these orbitals has a well-known form

$$H(\mathbf{k}) = t \sum_i (\sigma_x \cos \mathbf{k} \cdot \mathbf{a}_i - \sigma_y \sin \mathbf{k} \cdot \mathbf{a}_i), \quad (6)$$

where a_i are the three vectors connecting nearest neighbors, and $\sigma_{x,y}$ are Pauli matrices. With $t = -2.7$ eV this Hamiltonian approximates well the graphene band structure at energies close to the Dirac points, as a comparison to the DFT calculations shows [36].

C. IACA and MS photoemission models for graphene

Let us start with atomlike photoionization profiles for C atoms in graphene. With the light incidence along the surface normal, dipole selection rules require the $Y_1^0 \rightarrow Y_2^{\pm 1}$ for C_{\pm} light. Hence, circular dichroism in angular distribution (CDAD) vanishes (see Supplemental Material [33] for details). The situation is different if the light incidence is not aligned with the orbital quantization axis, as shown in Figs. 2(a)–2(e). Treatment of this case requires either a decomposition of the orbital along the quantization axis defined by the light incidence [71] or decomposition of light polarization vector along the z axis [53], with both $l \pm 1$ channels being allowed and interfering. The intensity profile depends on the radial integrals and phase shifts between the $l - 1$ and $l + 1$ scattering states, both depending on the kinetic energy [72]. The intensity profiles in Figs. 2(a)–2(b) depend on the light chirality and produce the CDAD pattern shown in Fig. 2(c), a result known from atomic physics [22].

The initial-state tight-binding wave function of graphene can be written as $\psi(\mathbf{k}) = A(\mathbf{k}_{\parallel})|C_A\rangle + B(\mathbf{k}_{\parallel})|C_B\rangle$, where $|C_A\rangle$ and $|C_B\rangle$ are atomlike C $2p$ Y_1^0 wave functions centered on the two nonequivalent sites within the unit cell, with complex coefficients $A(\mathbf{k}_{\parallel})$ and $B(\mathbf{k}_{\parallel})$. The transition matrix element can be written as

$$M_{fi}(\mathbf{k}_f) \propto [A(\mathbf{k}_{\parallel}) \cdot M_A(\mathbf{k}_f) + B(\mathbf{k}_{\parallel}) \cdot M_B(\mathbf{k}_f)] \times \delta(h\nu - E_k - W - E_B), \quad (7)$$

where E_B is the binding energy, W the work function, and \mathbf{k}_f indicates the detected far-field photoelectron with kinetic energy $E_k = (2m/\hbar)|\mathbf{k}_f|^2$ and emitted along the direction $\mathbf{k}_f/|\mathbf{k}_f|$.

With MS, the photoemission matrix element becomes

$$M_{fi,MS}(\mathbf{k}_f) \propto [A(\mathbf{k}_{\parallel}) \cdot M_{A,MS}(\mathbf{k}_f) + B(\mathbf{k}_{\parallel}) \cdot M_{B,MS}(\mathbf{k}_f)] \times \delta(h\nu - E_k - W - E_B), \quad (8)$$

where the patterns shown in Figs. 3(a)–3(d) need to be added coherently; thus, their amplitudes and phases, as well as different positions of emitters A and B , are taken into account.

D. Details of calculation procedures

Real-space calculations were performed using the EDAC photoelectron diffraction computer code [26]. For the atomic patterns shown in Figs. 1(a)–1(e) and 5(a)–5(f) we used an inner potential of $V_0 = 0$ eV and muffin-tin potentials for the atoms in the cluster (touching muffin tins). For the radial wave function of C $2p$ we used values tabulated in Ref. [73], while for W $5d$ the radial wave function was calculated internally by EDAC. Spherical clusters centered at the emitter site were used. For W $5d$ we used the cluster radius of $R_{\max} = 15$ Å, with 463 atoms spread through 3 layers of WSe₂. For graphene we used $R_{\max} = 20$ Å, cluster consisting 481 atoms. The inelastic mean-free path of 5 Å was used in all cases. A surface barrier is simulated by the inner potential V_0 , where we have used $V_0 = 17$ eV for graphene and $V_0 = 13$ eV [42] for WSe₂, however, changing these values by a few eV does not change the calculated CD-ARPES maps considerably. Details on convergence of the EDAC calculations are provided in Supplemental Material [33].

One-step model calculations of graphene shown in Fig. 4 were performed using the OMNI code with a setup used previously [27]. Our photoemission calculations do not take substrate-related effects into account.

Differential cross section (DCS) and Sherman function computation for the electron scattering on W atom have been performed using the ELSEPA code [44]. The results shown in Figs. 6(h) and 6(j) have been calculated without taking into account correlation effects. Virtually the same results have been obtained with an atomic potential and with a muffin-tin potential with radius $R_{MT} = 1.35$ Å. Adding electron correlation on the level of the local density approximation (LDA), as implemented in ELSEPA, leads to small changes in the shapes of DCS and Sherman function, but does not qualitatively change the results.

E. Sample preparation and photoemission measurements

The measurements on graphene were performed at the NanoESCA beam line at Elettra using the modified Focus NanoESCA momentum microscope. The resolution was $\Delta E \approx 100$ meV and $\Delta k \approx 0.06$ Å⁻¹, the photon beam was incident at 65° with respect to the surface normal. The spectrometer system allows probing the momentum space up to a radius of ≈ 2.5 Å⁻¹ with respect to the Brillouin zone center. Samples were kept at ≈ 100 K. A dry transfer technique was used to prepare graphene/hBN heterostructures, the lateral sizes of the graphene flakes were ≈ 20 μm, thus matching the photon beam spot of ≈ 20 μm at NanoESCA. The twist angle between graphene and hBN was $\approx 20^\circ$. Details are provided in Supplemental Material [33].

WSe₂ and PtTe₂ measurements were performed on cleaved bulk single crystals at the PHELIX beam line at Solaris [74] at ≈ 40 K. The SPECS Phoibos 225 spectrometer resolution was set to <50 meV and all the maps were collected using the lens deflector system without rotating the sample during the measurement, thus probing the same sample area for each map. The end station at PHELIX employs the magic angle of 54.7° between the light incidence and the axis of the analyzer lens. Therefore, in the normal emission geometry, that is,

when the surface normal coincides with the spectrometer lens axis, the light incidence is at 54.7° , while at normal light incidence the axis of the spectrometer lens is at 54.7° off normal. The electrostatic lens deflector system of the analyzer allows scanning $\pm 17^\circ$ angle in both directions without rotating the sample.

GdMn₆Sn₆ measurements were performed at the micro-ARPES branch of the MAESTRO beam line at the Advanced Light Source. Sample was cleaved by the ceramic post method, and the experiments were performed at ≈ 20 K, where the sample is in the magnetic state, however, with the beam spot of > 10 μm we have been likely averaging over magnetic domains.

ACKNOWLEDGMENTS

We would like to thank S. Nemsak for fruitful discussions, F. J. Garcia de Abajo for making the EDAC code available, and C. Jozwiak, A. Bostwick, and E. Rotenberg for the assistance at the MAESTRO beam line at ALS. H.B. was supported by the DFG via the Project No. PL 712/5-1. X.H. was supported by Deutsche Forschungsgemeinschaft (DFG, German Research Foundation) under Germany's Excellence Strategy-Cluster of Excellence Matter and Light for Quantum Computing (ML4Q) Grant No. EXC 2004/1 - 390534769. M.Q. was supported by the Federal Ministry of Education and

Research of Germany in the framework of the Palestinian-German Science Bridge (BMBF Grant No. 01DH16027). Y.M. acknowledges support by the EIC Pathfinder OPEN Grant No. 101129641 "OBELIX" and by the DFG Grant No. TRR 288-422213477 (Project B06). K.J., T.W., J.M.C., and F.L. acknowledge funding from the Deutsche Forschungsgemeinschaft (DFG, German Research Foundation) within the Priority Programme SPP 2244 (Projects No. 443416235 and No. 443405092). J.M.C. acknowledges funding from the Alexander von Humboldt Foundation. F.L. acknowledges funding from the Emmy Noether Programme of the DFG (Project No. 511561801) and Germany's Excellence Strategy-Cluster of Excellence Matter and Light for Quantum Computing (ML4Q) through an Independence Grant. F.L. and F.S.T. acknowledge funding from the Bavarian Ministry of Economic Affairs, Regional Development and Energy within Bavaria's High-Tech Agenda Project "Bausteine für das Quantencomputing auf Basis topologischer Materialien mit experimentellen und theoretischen Ansätzen." This publication was partially developed under the provision of the Polish Ministry and Higher Education project "Support for research and development with the use of research infra-structure of the National Synchrotron Radiation Centre SOLARIS" under Contract No. 1/SOL/2021/2. We acknowledge SOLARIS Centre for the access to the PHELIX beam line, where part of the measurements were performed.

-
- [1] D. Go, D. Jo, H.-W. Lee, M. Kläui, and Y. Mokrousov, Orbital currents in solids, *Europhys. Lett.* **135**, 37001 (2021).
- [2] D. G. Ovalle, A. Pezo, and A. Manchon, Orbital Kerr effect and terahertz detection via the nonlinear Hall effect, *Phys. Rev. B* **110**, 094439 (2024).
- [3] Y. K. Kato, R. C. Myers, A. C. Gossard, and D. D. Awschalom, Observation of the spin Hall effect in semiconductors, *Science* **306**, 1910 (2004).
- [4] J.-H. Park, C. H. Kim, J.-W. Rhim, and J. H. Han, Orbital Rashba effect and its detection by circular dichroism angle-resolved photoemission spectroscopy, *Phys. Rev. B* **85**, 195401 (2012).
- [5] S. R. Park, J. Han, C. Kim, Y. Y. Koh, C. Kim, H. Lee, H. J. Choi, J. H. Han, K. D. Lee, N. J. Hur, M. Arita, K. Shimada, H. Namatame, and M. Taniguchi, Chiral orbital-angular momentum in the surface states of Bi₂Se₃, *Phys. Rev. Lett.* **108**, 046805 (2012).
- [6] Y. H. Wang, D. Hsieh, D. Pilon, L. Fu, D. R. Gardner, Y. S. Lee, and N. Gedik, Observation of a warped helical spin texture in Bi₂Se₃ from circular dichroism angle-resolved photoemission spectroscopy, *Phys. Rev. Lett.* **107**, 207602 (2011).
- [7] J. Jiang, F. Tang, X. C. Pan, H. M. Liu, X. H. Niu, Y. X. Wang, D. F. Xu, H. F. Yang, B. P. Xie, F. Q. Song, P. Dudin, T. K. Kim, M. Hoesch, P. K. Das, I. Vobornik, X. G. Wan, and D. L. Feng, Signature of strong spin-orbital coupling in the large nonsaturating magnetoresistance material WTe₂, *Phys. Rev. Lett.* **115**, 166601 (2015).
- [8] M. Schüler, U. D. Giovannini, H. Hübener, A. Rubio, M. A. Sentef, and P. Werner, Local Berry curvature signatures in dichroic angle-resolved photoelectron spectroscopy from two-dimensional materials, *Sci. Adv.* **6**, eaay2730 (2020).
- [9] S. Cho, J.-H. Park, J. Hong, J. Jung, B. S. Kim, G. Han, W. Kyung, Y. Kim, S.-K. Mo, J. D. Denlinger, J. H. Shim, J. H. Han, C. Kim, and S. R. Park, Experimental observation of hidden Berry curvature in inversion-symmetric bulk 2H-WSe₂, *Phys. Rev. Lett.* **121**, 186401 (2018).
- [10] S. Cho, J.-H. Park, S. Huh, J. Hong, W. Kyung, B.-G. Park, J. D. Denlinger, J. H. Shim, C. Kim, and S. R. Park, Studying local Berry curvature in 2H-WSe₂ by circular dichroism photoemission utilizing crystal mirror plane, *Sci. Rep.* **11**, 1684 (2021).
- [11] Y. Ohtsubo, T. Nakaya, T. Nakamura, P. Le Fèvre, F. Bertran, F. Iga, and S.-I. Kimura, Breakdown of bulk-projected isotropy in surface electronic states of topological Kondo insulator SmB₆(001), *Nat. Commun.* **13**, 5600 (2022).
- [12] F. Mazzola, W. Brzezicki, M. T. Mercaldo, A. Guarino, C. Bigi, J. A. Miwa, D. De Fazio, A. Crepaldi, J. Fujii, G. Rossi, P. Orgiani, S. K. Chaluvadi, S. P. Chalil, G. Panaccione, A. Jana, V. Polewczyk, I. Vobornik, C. Kim, F. Miletto-Granozio, R. Fittipaldi *et al.*, Signatures of a surface spin-orbital chiral metal, *Nature (London)* **626**, 752 (2024).
- [13] O. Fedchenko, J. Minár, A. Akashdeep, S. W. D'Souza, D. Vasilyev, O. Tkach, L. Odenbreit, Q. Nguyen, D. Kutnyakhov, N. Wind, L. Wenthous, M. Scholz, K. Rosnagel, M. Hoesch, M. Aeschlimann, B. Stadtmüller, M. Kläui, G. Schönhense, T. Jungwirth, A. B. Hellenes *et al.*, Observation of time-reversal symmetry breaking in the band structure of altermagnetic RuO₂, *Sci. Adv.* **10**, eadj4883 (2024).
- [14] J. Erhardt, C. Schmitt, P. Eck, M. Schmitt, P. Keßler, K. Lee, T. Kim, C. Cacho, I. Cojocariu, D. Baranowski, V. Feyer, L.

- Veyrat, G. Sangiovanni, R. Claessen, and S. Moser, Bias-free access to orbital angular momentum in two-dimensional quantum materials, *Phys. Rev. Lett.* **132**, 196401 (2024).
- [15] H. Hayashi, D. Go, S. Haku, Y. Mokrousov, and K. Ando, Observation of orbital pumping, *Nat. Electron.* **7**, 646 (2024).
- [16] D. Go, D. Jo, C. Kim, and H.-W. Lee, Intrinsic spin and orbital Hall effects from orbital texture, *Phys. Rev. Lett.* **121**, 086602 (2018).
- [17] J. Sohn, J. M. Lee, and H.-W. Lee, Dyakonov-Perel-like orbital and spin relaxations in centrosymmetric systems, *Phys. Rev. Lett.* **132**, 246301 (2024).
- [18] M. Berritta, R. Mondal, K. Carva, and P. M. Oppeneer, *Ab initio* theory of coherent laser-induced magnetization in metals, *Phys. Rev. Lett.* **117**, 137203 (2016).
- [19] O. Busch, F. Ziolkowski, I. Mertig, and J. Henk, Ultrafast dynamics of orbital angular momentum of electrons induced by femtosecond laser pulses: Generation and transfer across interfaces, *Phys. Rev. B* **108**, 104408 (2023).
- [20] T. S. Seifert, D. Go, H. Hayashi, R. Rouzegar, F. Freimuth, K. Ando, Y. Mokrousov, and T. Kampfrath, Time-domain observation of ballistic orbital-angular-momentum currents with giant relaxation length in tungsten, *Nat. Nanotechnol.* **18**, 1132 (2023).
- [21] K. Nukui, S. Iihama, K. Ishibashi, S. Yamashita, A. Sakuma, P. Scheid, G. Malinowski, M. Hehn, S. Mangin, and S. Mizukami, Light-induced torque in ferromagnetic metals via orbital angular momentum generated by photon-helicity, *Phys. Rev. Lett.* **134**, 016701 (2025).
- [22] R. L. Dubs, S. N. Dixit, and V. McKoy, Circular dichroism in photoelectron angular distributions from adsorbed atoms, *Phys. Rev. B* **32**, 8389 (1985).
- [23] M. V. Berry, The quantum phase, five years after, in *Geometric Phases in Physics*, edited by F. Wilczek and A. Shapere (World Scientific, Singapore, 1989), pp. 3–28.
- [24] A. Gianfrate, O. Bleu, L. Dominici, V. Ardizzone, M. De Giorgi, D. Ballarini, G. Lerario, K. W. West, L. N. Pfeiffer, D. D. Solnyshkov, D. Sanvitto, and G. Malpuech, Measurement of the quantum geometric tensor and of the anomalous Hall drift, *Nature (London)* **578**, 381 (2020).
- [25] M. Kang, S. Kim, Y. Qian, P. M. Neves, L. Ye, J. Jung, D. Puntel, F. Mazzola, S. Fang, C. Jozwiak, A. Bostwick, E. Rotenberg, J. Fuji, I. Vobornik, J.-H. Park, J. G. Checkelsky, B.-J. Yang, and R. Comin, Measurements of the quantum geometric tensor in solids, *Nat. Phys.* **21**, 110 (2025).
- [26] F. J. García de Abajo, M. A. Van Hove, and C. S. Fadley, Multiple scattering of electrons in solids and molecules: A cluster-model approach, *Phys. Rev. B* **63**, 075404 (2001).
- [27] I. Gierz, J. Henk, H. Höchst, C. R. Ast, and K. Kern, Illuminating the dark corridor in graphene: Polarization dependence of angle-resolved photoemission spectroscopy on graphene, *Phys. Rev. B* **83**, 121408(R) (2011).
- [28] E. Krasovskii, One-step theory view on photoelectron diffraction: Application to graphene, *Nanomaterials* **12**, 4040 (2022).
- [29] P. Krüger and F. Matsui, Observation and theory of strong circular dichroism in angle-resolved photoemission from graphite, *J. Electron Spectrosc. Relat. Phenom.* **258**, 147219 (2022).
- [30] S. Beaulieu, J. Schusser, S. Dong, M. Schüler, T. Pincelli, M. Dendzik, J. Maklar, A. Neef, H. Ebert, K. Hricovini, M. Wolf, J. Braun, L. Rettig, J. Minár, and R. Ernstorfer, Revealing hidden orbital pseudospin texture with time-reversal dichroism in photoelectron angular distributions, *Phys. Rev. Lett.* **125**, 216404 (2020).
- [31] J. Schusser, H. Orio, M. Ünzelmann, J. Heßdörfer, M. P. T. Masilamani, F. Diekmann, K. Rossnagel, and F. Reinert, Towards robust dichroism in angle-resolved photoemission, *Commun. Phys.* **7**, 270 (2024).
- [32] H. Daimon, T. Nakatani, S. Imada, S. Suga, Y. Kagoshima, and T. Miyahara, Strong circular dichroism in photoelectron diffraction from nonchiral, nonmagnetic material—direct observation of rotational motion of electrons, *Jpn. J. Appl. Phys.* **32**, L1480 (1993).
- [33] See Supplemental Material at <http://link.aps.org/supplemental/10.1103/PhysRevB.111.115127> for the details of experimental and theoretical methods, which includes Refs. [75–78].
- [34] *Solid-State Photoemission and Related Methods*, edited by W. Schattke and M. A. Van Hove (Wiley, Weinheim, Germany, 2003), Sec. 2.7.
- [35] P. Krüger, F. Da Pieve, and J. Osterwalder, Real-space multiple scattering method for angle-resolved photoemission and valence-band photoelectron diffraction and its application to Cu(111), *Phys. Rev. B* **83**, 115437 (2011).
- [36] S. Reich, J. Maultzsch, C. Thomsen, and P. Ordejón, Tight-binding description of graphene, *Phys. Rev. B* **66**, 035412 (2002).
- [37] C. S. Kern, A. Haags, L. Egger, X. Yang, H. Kirschner, S. Wolff, T. Seyller, A. Gottwald, M. Richter, U. De Giovannini, A. Rubio, M. G. Ramsey, F. C. Bocquet, S. Soubatch, F. S. Tautz, P. Puschnig, and S. Moser, Simple extension of the plane-wave final state in photoemission: Bringing understanding to the photon-energy dependence of two-dimensional materials, *Phys. Rev. Res.* **5**, 033075 (2023).
- [38] Y. Liu, G. Bian, T. Miller, and T.-C. Chiang, Visualizing electronic chirality and Berry phases in graphene systems using photoemission with circularly polarized light, *Phys. Rev. Lett.* **107**, 166803 (2011).
- [39] F. Matsui, H. Nishikawa, H. Daimon, M. Muntwiler, M. Takizawa, H. Namba, and T. Greber, The $4\pi k_z$ periodicity in photoemission from graphite, *Phys. Rev. B* **97**, 045430 (2018).
- [40] D. Sébilleau, R. Gunnella, Z.-Y. Wu, S. D. Matteo, and C. R. Natoli, Multiple-scattering approach with complex potential in the interpretation of electron and photon spectroscopies, *J. Phys.: Condens. Matter* **18**, R175 (2006).
- [41] T. Matsushita, F. Matsui, H. Daimon, and K. Hayashi, Photoelectron holography with improved image reconstruction, *J. Electron Spectrosc. Relat. Phenom.* **178-179**, 195 (2010).
- [42] J. Riley, F. Mazzola, M. Dendzik, M. Michiardi, T. Takayama, L. Bawden, C. Granerød, M. Leandersson, T. Balasubramanian, M. Hoesch, T. K. Kim, H. Takagi, W. Meevasana, P. Hofmann, M. S. Bahramy, J. W. Wells, and P. D. C. King, Direct observation of spin-polarized bulk bands in an inversion-symmetric semiconductor, *Nat. Phys.* **10**, 835 (2014).
- [43] R. Sagehashi, G. Park, and P. Krüger, Theory of circular dichroism in angle-resolved resonant photoemission from magnetic surfaces, *Phys. Rev. B* **107**, 075407 (2023).
- [44] F. Salvat, A. Jablonski, and C. J. Powell, ELSEPA—Dirac partial-wave calculation of elastic scattering of electrons and positrons by atoms, positive ions and molecules (New Version Announcement), *Comput. Phys. Commun.* **261**, 107704 (2021).

- [45] K. Jost, F. Kaussen, and J. Kessler, Efficient low-energy Mott analyser in comparison with other methods for polarisation analysis, *J. Phys. E: Sci. Instrum.* **14**, 735 (1981).
- [46] M. Gehlmann, I. Aguilera, G. Bihlmayer, E. Młyńczak, M. Eschbach, S. Döring, P. Gospodarič, S. Cramm, B. Kardynał, L. Plucinski, S. Blügel, and C. M. Schneider, Quasi 2D electronic states with high spin-polarization in centrosymmetric MoS₂ bulk crystals, *Sci. Rep.* **6**, 26197 (2016).
- [47] D. Gregory and M. Fink, Theoretical electron scattering amplitudes and spin polarizations: Electron energies 100 to 1500 eV Part III. Li, Na, Mg, P, K, Ca, Sc, Mn, Ga, Br, Sr, Mo, Rh, Cd, Ba, W, and Os targets, *At. Data Nucl. Data Tables* **14**, 39 (1974).
- [48] J. Kessler, *Polarized Electrons* (Springer, Berlin, 1985).
- [49] Z. Liu, N. Zhao, M. Li, Q. Yin, Q. Wang, Z. Liu, D. Shen, Y. Huang, H. Lei, K. Liu, and S. Wang, Electronic correlation effects in the kagome magnet GdMn₆Sn₆, *Phys. Rev. B* **104**, 115122 (2021).
- [50] M. Masilamani, J. Schusser, M. Qahosh, L. Plucinski, and F. Reinert, One-step model photoemission calculations of Type-II Dirac semimetal PtTe₂, *AIP Conf. Proc.* **3054**, 070004 (2024).
- [51] M. Yan, H. Huang, K. Zhang, E. Wang, W. Yao, K. Deng, G. Wan, H. Zhang, M. Arita, H. Yang, Z. Sun, H. Yao, Y. Wu, S. Fan, W. Duan, and S. Zhou, Lorentz-violating type-II Dirac fermions in transition metal dichalcogenide PtTe₂, *Nat. Commun.* **8**, 257 (2017).
- [52] M. Bahramy, O. Clark, B.-J. Yang, J. Feng, L. Bawden, J. Riley, I. Marković, F. Mazzola, V. Sunko, D. Biswas, S. Cooil, M. Jorge, J. Wells, M. Leandersson, T. Balasubramanian, J. Fujii, I. Vobornik, J. E. Rault, T. Kim, M. Hoesch *et al.*, Ubiquitous formation of bulk Dirac cones and topological surface states from a single orbital manifold in transition-metal dichalcogenides, *Nat. Mater.* **17**, 21 (2018).
- [53] S. Moser, An experimentalist's guide to the matrix element in angle resolved photoemission, *J. Electron Spectrosc. Relat. Phenom.* **214**, 29 (2017).
- [54] J. Sánchez-Barriga, A. Varykhalov, J. Braun, S.-Y. Xu, N. Alidoust, O. Kornilov, J. Minár, K. Hummer, G. Springholz, G. Bauer, R. Schumann, L. V. Yashina, H. Ebert, M. Z. Hasan, and O. Rader, Photoemission of Bi₂Se₃ with circularly polarized light: Probe of spin polarization or means for spin manipulation? *Phys. Rev. X* **4**, 011046 (2014).
- [55] T. Heider, G. Bihlmayer, J. Schusser, F. Reinert, J. Minár, S. Blügel, C. M. Schneider, and L. Plucinski, Geometry-induced spin filtering in photoemission maps from WTe₂ surface states, *Phys. Rev. Lett.* **130**, 146401 (2023).
- [56] W. Shockley, On the surface states associated with a periodic potential, *Phys. Rev.* **56**, 317 (1939).
- [57] J. Henk, W. Schattke, H. Carstensen, R. Manzke, and M. Skibowski, Surface-barrier and polarization effects in the photoemission from GaAs(110), *Phys. Rev. B* **47**, 2251 (1993).
- [58] J. Henk, A. M. N. Niklasson, and B. Johansson, Multiple-scattering theoretical approach to magnetic dichroism and spin polarization in angle-resolved core-level photoemission, *Phys. Rev. B* **59**, 13986 (1999).
- [59] T. Hühne, C. Zecha, H. Ebert, P. H. Dederichs, and R. Zeller, Full-potential spin-polarized relativistic Korringa-Kohn-Rostoker method implemented and applied to bcc Fe, fcc Co, and fcc Ni, *Phys. Rev. B* **58**, 10236 (1998).
- [60] R. C. Vidal, H. Bentmann, J. I. Facio, T. Heider, P. Kagerer, C. I. Fornari, T. R. F. Peixoto, T. Figgeimeier, S. Jung, C. Cacho, B. Büchner, J. van den Brink, C. M. Schneider, L. Plucinski, E. F. Schwier, K. Shimada, M. Richter, A. Isaeva, and F. Reinert, Orbital complexity in intrinsic magnetic topological insulators MnBi₄Te₇ and MnBi₆Te₁₀, *Phys. Rev. Lett.* **126**, 176403 (2021).
- [61] R. Takahashi and N. Nagaosa, Berry curvature and orbital angular momentum of electrons in angle-resolved photoemission spectroscopy, *Phys. Rev. B* **91**, 245133 (2015).
- [62] R. Resta, Macroscopic polarization in crystalline dielectrics: the geometric phase approach, *Rev. Mod. Phys.* **66**, 899 (1994).
- [63] R. Resta, Magnetic circular dichroism versus orbital magnetization, *Phys. Rev. Res.* **2**, 023139 (2020).
- [64] M. Altarelli, Comment on "Magnetic circular dichroism versus orbital magnetization", *Phys. Rev. Res.* **2**, 048001 (2020).
- [65] R. Resta, Reply to "Comment on 'Magnetic circular dichroism versus orbital magnetization'", *Phys. Rev. Res.* **2**, 048002 (2020).
- [66] P. Krüger, Photoelectron diffraction from valence states of oriented molecules, *J. Phys. Soc. Jpn.* **87**, 061007 (2018).
- [67] A. Liebsch, Theory of photoemission from localized adsorbate levels, *Phys. Rev. B* **13**, 544 (1976).
- [68] P. Blaha, K. Schwarz, F. Tran, R. Laskowski, G. K. H. Madsen, and L. D. Marks, WIEN2k: An APW+lo program for calculating the properties of solids, *J. Chem. Phys.* **152**, 074101 (2020).
- [69] W. D. Grobman, Angle-resolved photoemission from molecules in the independent-atomic-center approximation, *Phys. Rev. B* **17**, 4573 (1978).
- [70] S. Moser, A toy model for dichroism in angle resolved photoemission, *J. Electron Spectrosc. Relat. Phenom.* **262**, 147278 (2023).
- [71] R. L. Dubs, S. N. Dixit, and V. McKoy, Circular dichroism in photoelectron angular distributions from oriented linear molecules, *Phys. Rev. Lett.* **54**, 1249 (1985).
- [72] S. Goldberg, C. Fadley, and S. Kono, Photoionization cross-sections for atomic orbitals with random and fixed spatial orientation, *J. Electron Spectrosc. Relat. Phenom.* **21**, 285 (1981).
- [73] E. Clementi and C. Roetti, Roothaan-Hartree-Fock atomic wavefunctions: Basis functions and their coefficients for ground and certain excited states of neutral and ionized atoms, $Z \leq 54$, *At. Data Nucl. Data Tables* **14**, 177 (1974).
- [74] M. Szczepanik-Ciba, T. Sobol, and J. Szade, PHELIX—A new soft x-ray spectroscopy beamline at SOLARIS synchrotron, *Nucl. Instrum. Methods Phys. Res. Sect. B* **492**, 49 (2021).
- [75] R. P. Day, B. Zwartzenberg, I. S. Elfimov, and A. Damascelli, Computational framework *chinook* for angle-resolved photoemission spectroscopy, *npj Quantum Mater.* **4**, 54 (2019).
- [76] A. Liebsch, Theory of angular resolved photoemission from adsorbates, *Phys. Rev. Lett.* **32**, 1203 (1974).
- [77] J. Stohr and H. C. Siegmann, *Magnetism*, 2006th ed., Springer Series in Solid-State Sciences (Springer, Berlin, Germany, 2006).
- [78] J. Yeh and I. Lindau, Atomic subshell photoionization cross sections and asymmetry parameters: $1 \leq z \leq 103$, *At. Data Nucl. Data Tables* **32**, 1 (1985).